Optical imaging of tumor hypoxia dynamics

Gregory M. Palmer
Duke University Medical Center
Department of Radiation Oncology
P.O. Box 3455
Durham, North Carolina 27710

Andrew N. Fontanella
Duke University
Department of Biomedical Engineering
P.O. Box 3455
Durham, North Carolina 27710

Guoqing Zhang
University of Virginia
Department of Chemistry
P.O. Box 400319
Charlottesville, Virginia 22904

Gabi Hanna
Duke University Medical Center
Department of Radiation Oncology
P.O. Box 3455
Durham, North Carolina 27710

Cassandra L. Fraser
University of Virginia
Department of Chemistry
P.O. Box 400319
Charlottesville, Virginia 22904

Mark W. Dewhirst
Duke University Medical Center
Department of Radiation Oncology
    and
Duke University
Department of Biomedical Engineering
P.O. Box 3455
Durham, North Carolina 27710

Abstract. The influence of the tumor microenvironment and hypoxia plays a significant role in determining cancer progression, treatment response, and treatment resistance. That the tumor microenvironment is highly heterogeneous with significant intratumor and intertumor variability presents a significant challenge in developing effective cancer therapies. Critical to understanding the role of the tumor microenvironment is the ability to dynamically quantify oxygen levels in the vasculature and tissue in order to elucidate the roles of oxygen supply and consumption, spatially and temporally. To this end, we describe the use of hyperspectral imaging to characterize hemoglobin absorption to quantify hemoglobin content and oxygen saturation, as well as dual emissive fluorescent/phosphorescent boron nanoparticles, which serve as ratiometric indicators of tissue oxygen tension. Applying these techniques to a window-chamber tumor model illustrates the role of fluctuations in hemoglobin saturation in driving changes in tissue oxygenation, the two being significantly correlated ($r = 0.77$). Finally, a green-fluorescence-protein reporter for hypoxia inducible factor-1 (HIF-1) provides an endpoint for hypoxic stress in the tumor, which is used to demonstrate a significant association between tumor hypoxia dynamics and HIF-1 activity in an *in vivo* demonstration of the technique. © *2010 The International Society for Optical Engineering.* [DOI: 10.1117/1.3523363]

Tumor hypoxia plays an important role in cancer progression, metastasis, and the effectiveness of therapies.[1–3] It is a highly dynamic process and the temporal dynamics can play a significant role in treatment resistance and tumor aggressiveness.[2,4–10] A recent trend in therapeutic strategies is to target tumor angiogenesis in order to modify the microenvironment and make tumors more sensitive to conventional therapies.[11] The ability to measure pO_2 and image tumor hypoxia on the microscopic level is essential to further understanding microenvironmental factors and modifying therapies, depending on treatment response. Characterizing the local microenvironment, particularly hypoxia, longitudinally, on a microscopic scale would be ideal. This is a challenging problem, however, and one for which no established imaging technique exists. Many methods have been developed that range from histological staining with reducible nitroimidazole reagents, protein markers, and green fluorescence protein (GFP) or luciferase reporter genes, to electrochemical probe methods, and optical, nuclear medicine, and magnetic resonance techniques[12] although some methods are only suitable for the laboratory, others have been translated into the clinic, and all have their advantages and drawbacks.[13,14] The key point is that there is no easily implemented technique for imaging vascular oxygenation (hemoglobin oxygenation) in combination with tissue oxygen tension on the microcirculatory level. We present an approach based on hyperspectral imaging of hemoglobin absorption and dual emissive boron nanoparticles (BNPs). The combination of these techniques enables quantification of both oxygen supply (hemoglobin oxygen saturation) and tissue oxygen tension (BNPs ratiometric sensing).

Address all correspondence to: Gregory M. Palmer, Duke University, Department of Radiation Oncology, 288 MSRB 1, 203 Research Drive, P.O. Box 3455, Durham, North Carolina 27710; Tel: 919-613-5053; Fax: 919-684-8718; E-mail: greg.palmer@duke.edu

Recently, we reported a new kind of light-emitting biomaterial that offers many advantages for optical hypoxia imaging[15] Iodide-substituted difluoroboron dibenzoylmethane-polylactide (BF$_2$dbm(I)PLA) is multiemissive, exhibiting both short-lived fluorescence (F) and long-lived phosphorescence (P) after 1- or 2-photon excitation. Especially unique is the presence of P at room temperature (and 37°C) in these PLA biomaterials, even as BNPs in aqueous environments,[16] which makes them useful for O$_2$ sensing via a dynamic quenching mechanism. Many pO$_2$ sensors are based on lifetime (τ), because τ is a concentration-independent variable, but its measurement requires specialized instrumentation not typically present in routine fluorescence detection systems. More straightforward, however, is ratiometric sensing. A simple ratio of F/P intensities at the respective emission maxima provides information about relative O$_2$ levels, whereas calibration allows for absolute pO$_2$ measurement. Ratiometric methods also eliminate the effects of concentration and fluctuations in light intensity or detector sensitivity. Previously, ratiometry had been achieved with ternary mixtures of a cyanine dye standard and an O$_2$-sensitive Pt porphyrin phosphor in a sol gel matrix.[17] But single-component, dual-emissive BF$_2$dbm(I)PLA offers the additional advantages of greater sample homogeneity, minimal dye leaching, biocompatibility, and simplified processing; because the nanoparticle serves as both the standard (F) and the oxygen sensor (P) at once, should a sensor molecule degrade, intrinsically coupled F and P are equally affected. Furthermore, long P lifetimes ($\tau = \sim 5$ ms; compare to F: $\tau = 0.5$ ns) correlate with high oxygen sensitivity, making these materials especially well suited for hypoxia imaging. The second parameter of interest is vascular oxygenation, which can be obtained using hyperspectral imaging of transmitted light through the window chamber to characterize hemoglobin absorption as a function of wavelength. From these data, it is possible to extract the hemoglobin oxygen saturation within the microvasculature, as well as the product of hemoglobin concentration and path length, which is proportional to the total attenuation through the tissue. Finally, a HIF-1 reporter construct is expressed in the 4T1 cell line used in this study, which provides a direct measure of HIF-1 activity through induced expression of GFP.[18] This enables quantification of the biologic consequences of hypoxia on an important hypoxia-associated pathway that has been shown to influence treatment resistance and tumor aggressiveness.[10]

1 Methods and Materials

1.1 *BNP Preparation*

The dye-polymer conjugate[15] BF$_2$dbm(I)PLA and boron nanoparticle aqueous suspensions[16] were fabricated accordingly to previously reported methods at a concentration of 1 mg/ml. Specifically, the polymer was generated by solvent-free lactide ring opening polymerization using the primary alcohol functionalized BF$_2$dbm(I)OH initiator and tin octoate as the catalyst. Nanoprecipitation of N,N-dimethylformamide solutions of BF$_2$dbm(I)PLA into water, followed by dialysis and passage through filter paper, yields nanoparticles $\sim$80–100 nm diam.

1.2 *Microscope*

A Zeiss MPS intravital microscope was used for all imaging, using a 2.5X objective. A DAPI excitation filter cube was used for excitation, and a liquid-crystal tunable filter was used to isolate the emission wavelengths (Varispec, Cri Inc., Woburn, MA). This filter has a 10-nm bandwidth with an electronically controllable center wavelength. A CCD camera (AM1412, Digital Video Camera Company, Austin, TX) was then used to record images. For acquisition of BNP data, the DAPI excitation filter and mercury lamp source (HBO100, Carl Zeiss AG, Oberkochen, Germany) were used to excite the sample, with the emission recorded from 425 to 575 nm in 5-nm increments using 1-s exposures. This resulted in an 31-s acquisition time for oxygen tension maps. These were acquired in increments of 7.5 min, with brightfield hemoglobin saturation acquisitions acquired continuously in-between these (GFC Mass Flow Controller, Aalborg Inc., Orangeburg, NY). This was done to minimize exposure of tissue to UV light during the hour acquisition time. For brightfield imaging used for calculation of hemoglobin saturation, an unfiltered halogen white-light source was used in transmission mode through the window, with emission recorded from 520 to 620 nm in 10-nm increments.
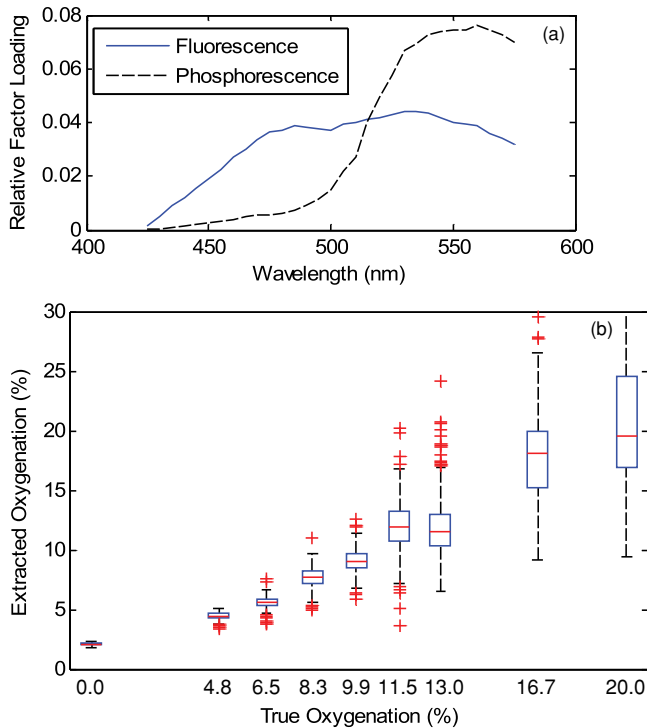
1.3 *BNP calibration*

The BNP solution was imaged in a 1-cm quartz cuvette with continuous bubbling of gas. The gas was a mixture of nitrogen and oxygen, with flow rates controlled by mass flow controllers (Aalborg, Inc.). The solution was initially purged of oxygen by bubbling with 100 N$_2$ for 30 min and then imaged using the setting described above. The oxygen flow was then incrementally increased to provide a range of oxygen concentration from 0 to 20%, with images taken at each increment after a 5-min stabilization period.

Calibration of BNP image data to absolute oxygen tension was performed as follows. First, the BNP calibration data taken from a pure BNP solution at various oxygen levels (described above) were preprocessed by normalizing them to their mean intensity. Next, they were spectrally decomposed using a two-component non-negative PARAFAC algorithm.[19] This yielded the component spectra of the fluorescence and phosphorescence emission, which can be seen in Fig. 1(a). The measured spectra of BNP emission can then be expressed as a linear combination of each of the two components using a non-negative least-squares fitting algorithm.[20] This provides the F and P component emission intensities, from which the F/P ratio was calculated. Finally, this was calibrated to absolute concentration using a second order Stern Volmer model, F/P $= a + b[O_2] + c[O_2]^2$. Figure 1(b) shows the results of this calibration, with the true oxygen concentration on the *x*-axis and the extracted oxygen concentration on the *y*-axis, shown as a boxplot. It was found that the responsiveness of the BNPs plateaus at $\sim$15% oxygen, with better accuracy at lower oxygen levels. The root-mean-square error on an independent testing data set was found to be 2.1 over the entire range, or 1.5 when including only oxygen levels of 15%.

1.4 *Window Chamber Model*

In vivo imaging was performed using a dorsal-skin-fold window-chamber model in a nude mouse (source, NCI Frederick).[21]

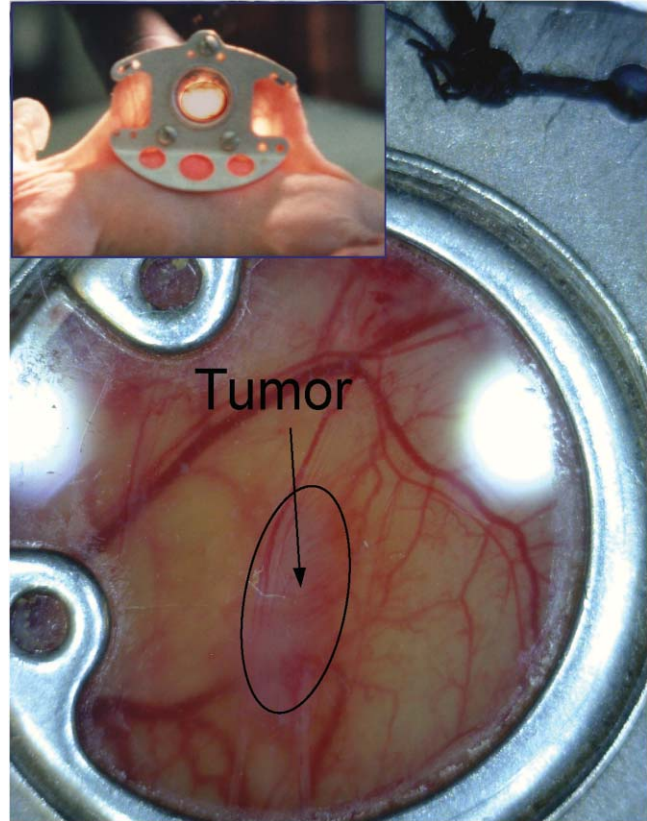Fig. 1 Component spectra (a) are shown for fluorescence and phosphorescence emission. In addition, (b) the accuracy of extraction of the percent of oxygen is shown for the calibration data, where it can be seen that there is tight correlation at lower values, with saturation occurring at ∼13% oxygen.

Fig. 2 The window-chamber model used in this study consists of a titanium metal frame, which holds the dorsal skin fold in place. The front skin flap is excised, and tumor cells are injected into the back plane of the opposing side skin and covered by a round coverglass. The inset shows the mouse with window implanted, with a larger view of the window itself. This is a different animal than that shown in the other figures.

Briefly, this consists of a titanium metal frame that is surgically implanted onto a dorsal skin fold. The frame holds the skin taught, and one face of the skin is surgically excised, exposing the underlying skin tissue, an example of which is shown in Fig. 2. Approximately 10,000 4T1 mammary carcinoma tumor cells were injected in 20 μL of Debucco's modified eagle medium (DMEM) via a 30-gauge syringe. These cells expressed constitutive red fluorescent protein (RFP), with HIF-1 inducible GFP expression.[18] Finally, a coverglass was placed over the tumor and secured with a retaining ring. The data presented were acquired from a single mouse. All animal work was approved by Duke University's Institutional Animal Care and Use Committee.

1.5 In Vivo Imaging

The mouse was anesthetized using 1.5% isoflurane mixed with medical air. The animal's temperature was maintained using a heated blanket. Breathing was monitored during imaging to ensure appropriate depth of anesthesia. First, a set of background images were acquired to characterize tissue autofluorescence. Next, ∼100 μL of the BNP solution was injected into the space between the window and tumor tissue to bathe the tissue, with excess fluid draining out the sides of the window, leaving a thin layer of BNP solution. Fluorescence images were acquired every 7.5 min for 1 h, with transmission images acquired continuously in-between fluorescence acquisitions.

1.6 Data Processing

Transmission images were processed using a modified form of existing techniques.[22] A modified form of Beer's law was used, which approximates attenuation through the tissue as a linear combination of absorption and scattering terms, namely

$$\log_{10}\left(\frac{I_0}{I}\right) = b_0 + b_1\mu_{\text{eff}} + \sum_i \varepsilon_i C_i, \qquad (1)$$

where I_0 is the transmission in the absence of tissue attenuation, which was measured using neutral density filters; b_0 is a constant term that accounts for variability in source intensity, specular reflection, or other heterogeneities in overall intensity; and μ_{eff} is the effective attenuation coefficient[23] derived from diffusion theory, $\mu_{\text{eff}} = \sqrt{3\mu_a(\mu_a + \mu_s')}$, calculated for representative skin optical properties at each wavelength,[24] and accounts for attenuation due to nonhemoglobin absorption and scattering. This was empirically found to provide a good fit to the nonvascular component of attenuation in tissue (for example, in the nonvascular regions of the images). ε_i is the wavelength-dependent molar extinction coefficient of each absorber in the model, and C_i is the product of its concentration and the effective path length. In this case, two absorbers, oxygenated (HbO$_2$) and deoxygenated (Hb) hemoglobin, were used. The use of this approximation
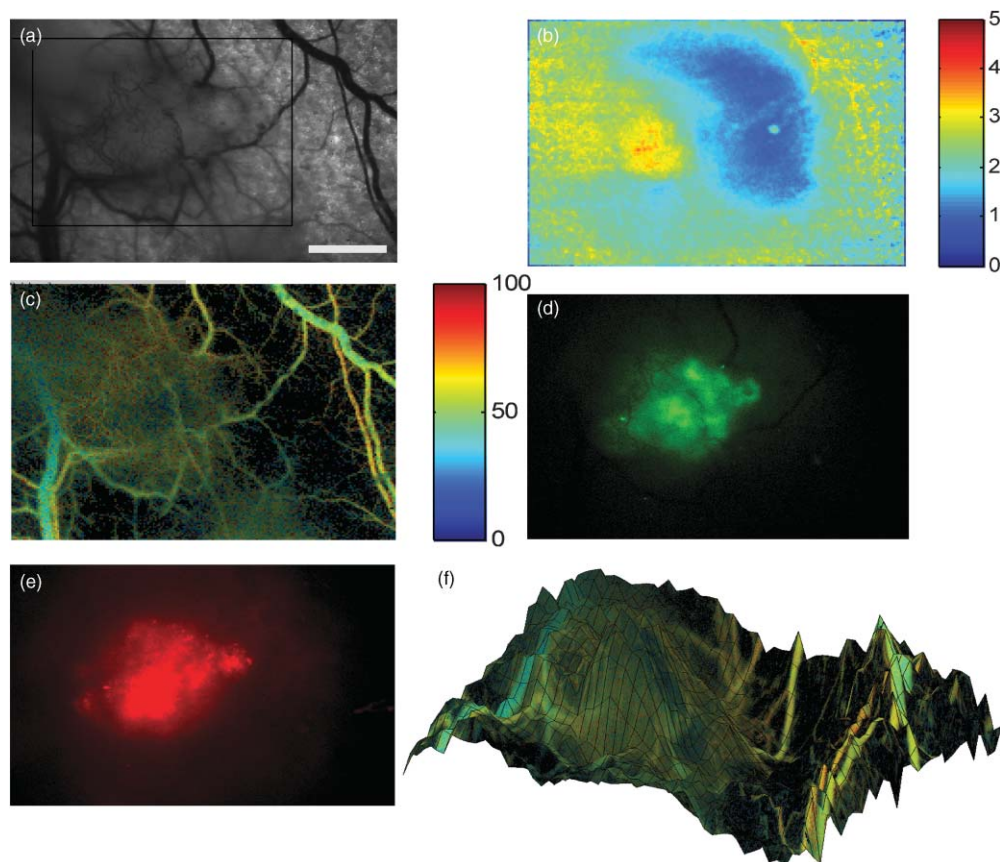
Fig. 3 (a) Bright field, (b) oxygen tension in the percent of oxygen, (c) hemoglobin oxygen saturation, (d) GFP-HIF-1 fluorescence, and (e) constitutively expressed RFP fluorescence are shown. The hemoglobin saturation (c) is shown with percent oxygen saturation on a color scale, whose brightness is modulated by the total hemoglobin content (thus, well-vascularized regions appear brighter). Also in (f), a combined plot shows the hemoglobin oxygen saturation plotted as in (c), with a 3-D projection of the tissue oxygenation shown on the vertical axis. The tumor is seen predominantly within the black box. These images were acquired toward the end of the imaging sequence ($t = 55$ min). Images are approximately 5×3.7 mm, with a 1-mm scale bar seen in (a).

enables rapid calculation of physiologic parameters, namely, hemoglobin content and saturation on a pixel-by-pixel basis. This equation is fit using a non-negative least-squares optimization algorithm over the measured wavelength range.[20] From this, the total hemoglobin content times the path length, $Hb_{tot} = C_{HbO_2} + C_{Hb}$ and the hemoglobin saturation, $Hb_{sat} = C_{HbO_2}/Hb_{tot}$ are calculated.

2 Results and Discussion

Figure 3 provides an example of optical data demonstrating quantitative imaging of tumor hypoxia and vascular function. Figure 3(a) shows a transmission image that allows for visualization of the tumor and its vasculature. Figure 3(b) depicts the oxygen tension as percent O_2 extracted from the BNP spectrum. These images reveal a region in the tumor with relatively high oxygen tension, while relatively low oxygen tension appears in the adjacent regions. This poorly oxygenated zone appears to be poorly vascularized and downstream of the tumor blood supply. Figure 3(c) shows the hemoglobin saturation on a color scale from blue (deoxygenated) to red (oxygenated). The color encoding at each pixel is then multiplied by the total hemoglobin content extracted from the same pixel, such that large vessels appear brighter, while nonvascularized pixels appear black, due

to low hemoglobin content. The tumor appears well vascularized with heterogeneous oxygenation. Figure 3(d) shows the GFP intensity, normalized to the peak value, which shows distinct pockets of intense GFP fluorescence within the central part of the tumor. Figure 3(e) shows the constitutively active RFP, showing the extent of the tumor. Finally, Fig. 3(f) shows a three-dimensional (3-D) visualization of the relationship among hemoglobin oxygen saturation, hemoglobin content, and tissue oxygen tension. The hemoglobin oxygen saturation color map is overlaid on a 3-D projection of the tissue oxygen tension plotted on the surface map, with the oxygen tension appearing on the vertical axis. Thus, oxygen gradients can be visualized as slopes on the plot, with a peak appearing on one side of the tumor close to the large artery on the lower left side, with a steep fall off on the trailing edge. Video 1 shows this rendering as it appears from a variety of angles.

A key advantage of both BNP emission and hemoglobin absorption-based hyperspectral imaging techniques is their ability to monitor dynamic changes over time. To this end, the parameters described for Fig. 3 were imaged semicontinuously for the course of 1 h. This enabled characterization the temporal dynamics of each parameter and allowed for their interrelationships to be studied. Figure 4(a) shows the Spearman rank correlation between the hemoglobin saturation and tissue oxygen
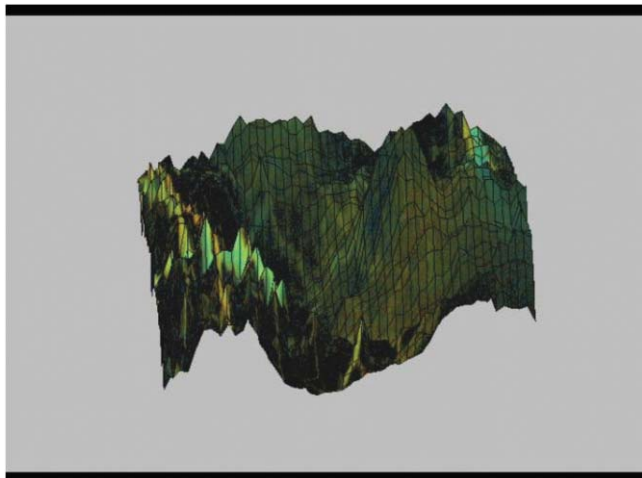
Video 1 The 3-D projection of tumor oxygen tension on the *z*-axis, along with hemoglobin saturation and total hemoglobin on the color scale identical to that shown in Fig. 3 (blue = deoxygenated → red = oxygenated, with the intensity modulated by the total hemoglobin content making vessels appear brighter). This enables visualization of gradients in tissue oxygen tension in relation to vessel morphology and oxygenation. It can be seen that the tumor oxygen tension is highly heterogeneous and has a steep gradient dividing a relatively well-oxygenated region from a relatively hypoxic region. (QuickTime, 2.6 MB).
[URL: http://dx.doi.org/10.1117/1.3523363.1]
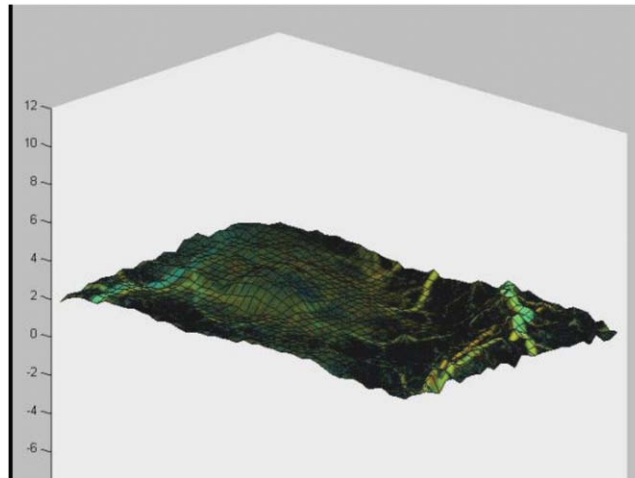
Video 2 Shows the dynamics of hemoglobin saturation and tumor oxygenation over an 1-h time period with oxygen tension shown as a 3-D projection along the *z*-axis, and hemoglobin saturation shown on a blue → red color scale identical to that in Fig. 3. Tissue oxygenation can be seen to be a dynamic process with constant variability throughout the time period. Hemoglobin saturation tracks well with changes in tissue oxygenation, with reddening vessels coinciding with increased oxygen tension. (QuickTime, 3.4 MB).
[URL: http://dx.doi.org/10.1117/1.3523363.2]

tension, pixel by pixel. Solid white regions indicate areas where the hemoglobin content was not sufficient to reconstruct the hemoglobin saturation. It can be seen that there is a tight correlation of hemoglobin oxygen saturation with tumor oxygenation (median $r = 0.77$). This correlation is relatively low; however, in the central tumor region, where instable flow and shunting is expected to occur. Figure 4(b) shows the pixel-by pixel standard deviation of tissue oxygenation over time, which indicates the magnitude of oxygen fluctuations over time. It can be seen that there are two distinct regions within the tumor, with the lower left quadrant showing distinctly greater fluctuations. This region is sandwiched between the large artery and vein in the lower left quadrant. The region to the right of the tumor shows consistently lower oxygen levels throughout the imaging period, and thus has relatively low standard deviation. Video 2 shows the dynamics of tissue oxygen tension and hemoglobin saturation over time, which illustrates these trends visually. Qualitatively, it can be seen that there are often rapid changes in hemoglobin saturation

(color scale), that coincide with more gradual changes in tissue oxygenation (*z*-axis height).

Finally, insofar as it is widely hypothesized that different microenvironmental phenotypes respond differently to various forms of treatment, one of the primary aims of this work was to evaluate the ability of these imaging techniques to segment tissues into different physiologic phenotypes based on the temporal dynamics of tissue oxygenation. To this end, the temporal oxygenation data were first decomposed using wavelet analysis. This is similar to Fourier analysis, which has previously been used to characterize temporal dynamics,[25] but has the advantage of being localized with respect to time as well as frequency,[26] and thus would better describe potentially abrupt or irregular changes in flow patterns. A decomposition was performed using a second-order Daubechies wavelet.[26] The discrete wavelet decomposition is applied at multiple levels, or scales. At the first level, the original signal is decomposed into an approximation and detail signal, where the detail signal is the convolution of the original signal and the wavelet function at the smallest scale or highest frequency. This essentially splits the signal into a
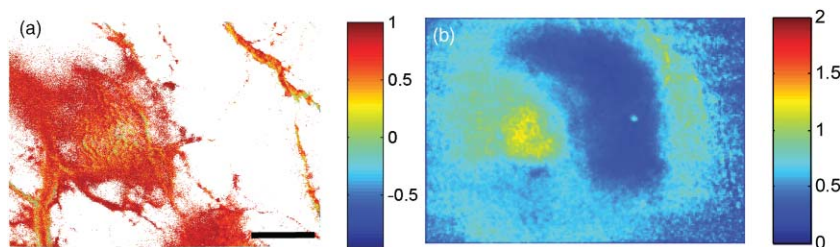
Fig. 4 (a) The Spearman rank correlation of hemoglobin oxygen saturation and tissue oxygen tension, which indicates that the central portion of the tumor has relatively low correlation between these parameters, indicating inefficiency of oxygen delivery to the tumor and possible shunting of flow. (b) The standard deviation of the tissue oxygen tension over the 1-h time period over which measurements were made, which indicates regions of the tumor that show the largest magnitude of fluctuations over time. A 1-mm scale bar is seen in (a).
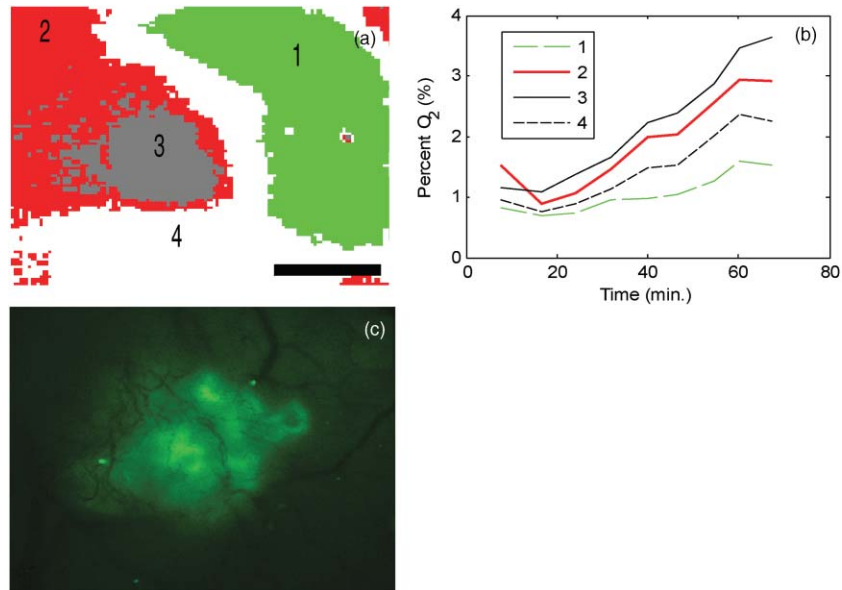
Fig. 5 Results of the clustering analysis shows (a) the spatial cluster assignment and (b) the median percent O$_2$ within each cluster. Also shown is the (c) HIF-1–induced GFP expression for the same tissue region. There is clear spatial segregation of the tumor and normal tissues, with the tumor being contained predominantly within clusters 2, 3, and 4. Note that this analysis was performed over a smaller region of interest indicated by the black box in Fig. 3(a). A 1-mm scale bar is seen in (a).

high-frequency component (detail) and low-frequency component (approximation), the sum of which yields the original signal. This process can be repeated with the scale of the wavelet function increasing by powers of 2 at each step, thus extracting lower and lower frequency components. In this case, a two-level decomposition was performed, which divides the temporal response into short- and long-period oscillations (center cycling periods of approximately 22.5 and 45 min). These coefficients were fed into a fuzzy c-means clustering algorithm[27] to identify which regions within and surrounding the tumor behaved most similarly over time. The fuzzy clustering algorithm classifies each tissue region according to the relative associations with each cluster centroid, allowing for the fact there is not a hard discrimination boundary between clusters; thus, cluster associations are assigned weights from 0 to 1. This was performed over a smaller region of interest containing only the tumor and immediately adjacent normal tissue as shown by the dark box in Fig. 3(a) to simplify this analysis. For the purpose of display, the maximum cluster association was selected for each pixel. Figure 5(a) shows a map of the maximum cluster association for each pixel, and Fig. 5(b) shows the median percent O$_2$ over time within each of these clusters. The tumor is contained predominantly within clusters 2, 3, and 4, with cluster 3 showing an earlier increase in oxygenation [see Fig. 5(b)] and also having a higher median value and larger variance over time [see Fig. 3(b)]. Interestingly, the bimodal distribution of GFP expression is also reflected in the distribution of clusters 3 and 4, which may reflect the influence of oxygen dynamics on HIF-1 activity. Specifically, cluster 3 has the largest fluctuations in oxygen tension [as seen in Figs 4(b) and 5(b), whereas cluster 4 has the lowest absolute oxygen tension [as seen in Fig. 5(b)], which have been shown to be two significant drivers of HIF-1 activity.[4] A pixel-by-pixel correlation of cluster 3 with GFP fluorescence intensity yields a Pearson correlation coefficient of 0.46

($p < 1 \times 10^{-15}$), indicating the significant correlation between cycling hypoxia dynamics and HIF-1 activity. The remaining clusters were not correlated with GFP fluorescence (correlation coefficients ranging between -0.14 and -0.09), which may be due in part to the fact that they all include significant normal tissue regions.

One of the limitations of this study is the Beer's law assumption for tissue attenuation. This is a common practice in interpreting wide-field hyperspectral imaging data sets, but it does not account for changes in path length with respect to wavelength and optical properties, or for the heterogeneity present in tissue. We are currently developing a Monte Carlo–based approach for interpreting such data and evaluating the errors induced through use of simplified modeling techniques. Another consideration in interpreting these data is the route of administration. Because the nanoparticles were applied topically, the sensing volume is limited to the superficial tissue space. It is unclear, based on this study, whether the nanoparticles are taken up by the cells or to what extent they penetrate into the tissue, but this could influence the measurement over time as the sensing volume changes. Because epi-illumination was used, along with a relatively short imaging duration (1 h), it is likely that the measurement is highly superficial throughout the measurement time. However, these fluctuations are more likely driven by true changes in tissue oxygenation than a change in penetration depth over time, given the high correlation coefficient seen between the independent measure of hemoglobin oxygen saturation. The time scale for these fluctuations in oxygenation is consistent with those measured previously using other methods.[4,25] In the future, confocal imaging or histology could be employed to gain a better understanding of the penetration depth of these nanoparticles over time, after topical application. In addition, for many clinical applications, a topical application may not be practical. For this reason, the use of intravenous administration has also

been considered and we have developed a PEGylated nanoparticle formulation that was found to accumulate near the tumor vasculature using confocal imaging.[28]

In conclusion, we have demonstrated and validated techniques by which vascular and tissue oxygenation can be imaged at high spatial and temporal resolution, enabling a detailed understanding of the tumor microenvironment and its influence on tumor gene expression. All these techniques are implemented using a simple modification to a standard fluorescent microscope, enabling a wide range of potential applications. There is no other technology that facilitates simultaneous measurement of vascular oxygen supply and tissue oxygen tension using a single instrument, and this work enables a significant advancement in our ability to characterize tissue hypoxia and its dynamic interactions *in vivo*. Hypoxia is a critical factor in a wide range of disease processes, including cancer, epilepsy, wound healing, and more. The capability of the techniques developed here to quickly, quantitatively, and nondestructively assess the dynamics of vascular oxygen supply and tissue oxygen tension could open up new possibilities for understanding of the basic mechanisms by which disease processes are influenced by hypoxia and correlating these to therapeutic response. In the future, we hope to translate these techniques to a clinical setting as a means of assessing tumor hypoxia and therapeutic response to evaluate their potential in guiding and monitoring therapy.

References

1. G. Lorusso and C. Rugg, "The tumor microenvironment and its contribution to tumor evolution toward metastasis," *Histochem. Cell Biol.* **130**(6), 1091–1103 (2008).
2. P. Vaupel, "Tumor microenvironmental physiology and its implications for radiation oncology," *Semin. Radiat. Oncol.* **14**(3), 198–206 (2004).
3. K. J. Williams, R. L. Cowen, and I. J. Stratford, "Hypoxia and oxidative stress in breast cancer—tumour hypoxia: therapeutic considerations," *Breast Cancer Res.* **3**(5), 328–331 (2001).
4. M. Dewhirst, "Relationships between cycling hypoxia, HIF-1, angiogenesis and oxidative stress," *Radiat. Res.* **172**(6), 653–665 (2009).
5. R. G. Bristow and R. P. Hill, "Hypoxia and metabolism: hypoxia, DNA repair and genetic instability," *Nat. Rev. Cancer.* **8**(3), 180–192 (2008).
6. J. M. Brown, "Evidence for acutely hypoxic cells in mouse tumours, and a possible mechanism of reoxygenation," *Br. J. Radiol.* **52**(620), 650–656 (1979).
7. P. Martinive, F. Defresne, C. Bouzin, J. Saliez, F. Lair, V. Gregoire, C. Michiels, C. Dessy, and O. Feron, "Preconditioning of the tumor vasculature and tumor cells by intermittent hypoxia: implications for anticancer therapies," *Cancer Res.* **66**(24), 11736–11744 (2006).
8. P. Martinive, F. Defresne, E. Quaghebeur, G. Daneau, N. Crokart, V. Gregoire, B. Gallez, C. Dessy, and O. Feron, "Impact of cyclic hypoxia on HIF-1alpha regulation in endothelial cells—new insights for antitumor treatments," *FEBS J.* **276**(2), 509–518 (2009).
9. M. W. Dewhirst, "Intermittent hypoxia furthers the rationale for hypoxia-inducible factor-1 targeting," *Cancer Res*. **67**(3), 854–855 (2007).
10. M. Dewhirst, Y. Cao, and B. Moeller, "Cycling hypoxia and free radicals regulate angiogenesis and radiotherapy response," *Nat. Rev. Cancer* **8**(6), 425–437 (2008).
11. R. K. Jain, "Normalization of tumor vasculature: an emerging concept in antiangiogenic therapy," *Science* **307**(5706), 58–62 (2005).
12. R. Springett and H. Swartz, "Measurements of oxygen in vivo: overview and perspectives on methods to measure oxygen within cells and tissues," *Antioxid. Redox Signal* **9**(8), 1295–1301 (2007).
13. M. W. Dewhirst, B. Klitzman, R. D. Braun, D. M. Brizel, Z. A. Haroon, and T. W. Secomb, "Review of methods used to study oxygen transport at the microcirculatory level," *Int. J. Cancer* **90**(5), 237–255 (2000).
14. A. R. Padhani, K. A. Krohn, J. S. Lewis, and M. Alber, "Imaging oxygenation of human tumours," *Eur. Radiol.* **17**(4), 861–872 (2007).
15. G. Zhang, G. M. Palmer, M. W. Dewhirst, and C. L. Fraser, "A dual-emissive-materials design concept enables tumour hypoxia imaging," *Nat. Mater.* **8**(9), 747–751 (2009).
16. A. Pfister, G. Zhang, J. Zareno, A. F. Horwitz, and C. L. Fraser, "Boron polylactide nanoparticles exhibiting fluorescence and phosphorescence in aqueous medium," *ACS Nano.* **2**(6), 1252–1258 (2008).
17. Y. E. L. Koo, Y. F. Cao, R. Kopelman, S. M. Koo, M. Brasuel, and M. A. Philbert, "Real-time measurements of dissolved oxygen inside live cells by organically modified silicate fluorescent nanosensors," *Anal. Chem.* **76**(9), 2498–2505 (2004).
18. B. J. Moeller, Y. Cao, C. Y. Li, and M. W. Dewhirst, "Radiation activates HIF-1 to regulate vascular radiosensitivity in tumors: role of reoxygenation, free radicals, and stress granules," *Cancer Cell* **5**(5), 429–441 (2004).
19. C. Andersson and R. Bro, "The N-way Toolbox for MATLAB," *Chemom. Intell. Lab. Syst.* **52**(1), 1–4 (2000).
20. R. Bro and S. DeJong, "A fast non-negativity-constrained least squares algorithm," *J. Chemom.* **11**(5), 393–401 (1997).
21. Q. Huang, S. Shan, R. D. Braun, J. Lanzen, G. Anyrhambatla, G. Kong, M. Borelli, P. Corry, M. W. Dewhirst, and C. Y. Li, "Noninvasive visualization of tumors in rodent dorsal skin window chambers," *Nat. Biotechnol.* **17**(10), 1033–1035 (1999).
22. B. S. Sorg, B. J. Moeller, O. Donovan, Y. Cao, and M. W. Dewhirst, "Hyperspectral imaging of hemoglobin saturation in tumor microvasculature and tumor hypoxia development," *J. Biomed. Opt.* **10**(4), 44004 (2005).
23. R. Splinter and B. A. Hooper, *An introduction to biomedical optics*, Taylor & Francis, New York (2007).
24. R. Huang and S. Jacques, "Skin optics summary" (1998); http://omlc.ogi.edu/news/jan98/skinoptics.html.
25. L. I. Cardenas-Navia, D. Mace, R. A. Richardson, D. F. Wilson, S. Shan, and M. W. Dewhirst, "The pervasive presence of fluctuating oxygenation in tumors," *Cancer Res*. **68**(14), 5812–5819 (2008).
26. J. S. Walker, *A primer on wavelets and their scientific applications*, Chapman & Hall/CRC, Boca Raton (2008).
27. F. Höppner, *Fuzzy cluster analysis : methods for classification, data analysis, and image recognition*, Wiley, Hoboken, NJ (1999).
28. F. Kersey, G. Zhang, G. Palmer, M. Dewhirst, and C. Fraser, "Stereocomplexed poly(lactic acid)-poly(ethylene glycol) nanoparticles with dual-emissive boron dyes for tumor accumulation," *ACS Nano.* (2010).